macQsimal	Title **Test and validation results for GHz imaging**	Deliverable Number **7.5**
Project Number **820393**		Version **1**

H2020-FETFLAG-2018-2021

macQsimal

Miniature Atomic vapor-Cell Quantum devices for SensIng and Metrology AppLications

Deliverable 7.5

Test and validation results for GHz imaging

WP 7 – Atomic GHz & THz sensors and vector imagers

Authors: Yongqi Shi, Philipp Treutlein

Lead participant: UNIBAS

Delivery date: 28.07.2022

Dissemination level: Public

Type: R (Document, Report)

This work has received funding from the European Union's Horizon 2020 research and innovation programme under grant agreement No. 820393.

Revision History

Author Name, Partner short name	Description	Date
Yongqi Shi (UNIBAS)	Draft 1	10.07.2022
Yongqi Shi (UNIBAS)	Draft 2	26.07.2022
Philipp Treutlein (UNIBAS)	Revision	26.07.2022
Yongqi Shi (UNIBAS)	Draft for review	27.07.2022
Andreia Cruz (accelCH)	Formal checks and formatting	28.07.2022

Abbreviations

CPW	Coplanar waveguide
EM	Electromagnetic
Eqn.	Equation
FDRS	Frequency-domain Rabi spectroscopy
Fig.	Figure
MEMS	Micro-electromechanical systems
MMIC	Monolithic microwave integrated circuits
MW	Microwave wave
Sec.	Section
SMA	Sub-Miniature A
TDRO	Time-domain Rabi oscillation
UV	Ultraviolet

Partner short names

CSEM	CSEM SA – Centre Suisse d'Électronique et de Microtechnique, CH
UDUR	University of Durham, UK
UNIBAS	Universität Basel, CH

Contents

Executive Summary

This deliverable describes test and validation results for GHz microwave magnetic field imaging with a MEMS atomic vapor cell. It is a follow-up report of the Deliverable 7.2 "Setup for high-resolution imaging of GHz fields", to meet Objective 4.1 of the macQsimal project. We developed and implemented an improved microwave field imaging scheme based on frequency domain Rabi spectroscopy and used it to image the field distribution of a $f_{MW} = \sim 15.05 GHz$ MW magnetic field on a coplanar waveguide. Due to the simultaneous imaging of the Rabi frequencies and detunings, the new method gets rid of the separate calibration measurement for the detuning needed in the traditional time-domain Rabi oscillation measurement, speeds up the data taking, and improves the accuracy of the MW imaging results. The demonstrated spatial resolution of the microwave field image is $\sim 80 \mu m \times 80 \mu m \times 200 \mu m$ and the sensitivity to the microwave magnetic field is $264 nT/\sqrt{Hz}$. The measured MW field distribution agrees well with a simulation.

1 Introduction

Monolithic microwave integrated circuits (MMICs) working in the microwave (MW) frequency range ($0.3-300GHz$) are core elements of many modern technologies, including 5G communications. Function-and-failure analysis of the MMICs circuits is critical for high-quality and high-throughput fabrication, while the conventional S-parameter (scattering-parameter) measurement method lacks specificity in monitoring defects and identifying the cause of malfunctions of the circuit that are not expected during the design stage.

Our group has developed a method using alkali atomic vapor cells for imaging the near-field MW magnetic field distribution above a MW circuit [1-4]. By comparing the measured field distributions with electromagnetic (EM) wave simulations, the causes of malfunctions and failures of the circuit can be more easily identified. So far, MW magnetic field imaging with atomic vapor cells has been demonstrated only near $6.8GHz$ [1-3], which is the ground state energy splitting of ^{87}Rb in a moderate static magnetic field (several Gausses). In [4], detection of a microwave magnetic field amplitude has been demonstrated at variable frequency using a strong static magnetic field for tuning the atomic transitions frequency. However, static field inhomogeneities prevented the imaging of a field distribution. Also, all of the demonstrated results use time-domain Rabi oscillations (TDRO) to measure the Rabi frequencies, i.e., the MW magnetic field amplitudes, in a spatially resolved way.

In this report, we demonstrate MW magnetic field imaging at a variable MW frequency based on frequency-domain Rabi spectroscopy (FDRS) in a micro-electromechanical system (MEMS) atomic vapor cell. We apply a strong static magnetic field ($\sim 5500Gauss$) to split the ground state energy levels so as to change the MW frequency to be imaged (here we choose a frequency of ~ 15 GHz for demonstration). The demonstrated spatial resolution is $\sim 80\mu m \times 80\mu m \times 200\mu m$ and the sensitivity is $264nT/\sqrt{Hz}$. The deliverable contains the following parts: Section 1 gives a brief introduction of MW magnetic field imaging with atomic vapor cell; Section 2 describes the current experimental setup and discusses the challenges in using TDRO, motivating the use of FDRS; Section 3 presents the first imaging result based on FDRS with a MEMS atomic vapor cell, as well as the sensitivity and the spatial resolution; and Section 4 is the conclusion.

2 Experimental setup

A detailed description and several important calibration measurements of the experimental setup have been reported in the former Deliverable 7.2, so here we focus on the requirements for using TDRO to image the MW field in the current setup. We first briefly explain the principle and prerequisite of TDRO, then show the static magnetic field distribution of the current setup (reported also in Deliverable 7.2), and discuss the challenges it presents for TDRO. We also present the ultra-thin MEMS atomic vapor cell that was fabricated in macQsimal, resulting in a more homogeneous magnetic field along the laser propagation direction.

2.1 Requirements for Time-domain Rabi oscillations

We use ground state MW transitions of the Rb atoms to measure the MW magnetic field distribution. The interaction between the input MW magnetic field and the corresponding two levels of ground state Rb atoms at position (x, y) (xy-plane is orthogonal to the laser propagation direction) in the atomic vapor cell can be described as,

$$\Delta p(x,y) = \frac{\Omega_{Rabi}(x,y)^2}{\Omega_{Rabi}(x,y)^2+\delta(x,y)^2} \sin^2\left(\frac{1}{2}\sqrt{\Omega_{Rabi}(x,y)^2+\delta(x,y)^2}\cdot \Delta t_{MW}\right), \qquad (1)$$

where $\Delta p(x,y) = p_2(x,y) - p_1(x,y)$ is the population imbalance between the two ground states induced by the microwave, $\Omega_{Rabi}(x,y) \propto B_{MW}(x,y)$ is the local Rabi frequency that is proportional to the local MW magnetic field to be measured, $\delta(x,y) = \omega_0(x,y) - 2\pi \cdot f_{MW}$ is the detuning between the applied MW frequency f_{MW} and the local energy splitting between the two ground states $\omega_0(x,y)$ given by the local static magnetic field $B_{DC}(x,y)$ according to Breit-Rabi formula, and Δt_{MW} is the MW pulse duration.

First, a pump laser pulse is used to build up an initial population imbalance. The MW pulse is applied right after the pump pulse. When scanning the MW pulse duration Δt_{MW} the population difference $\Delta p(x,y)$ performs Rabi oscillations at an oscillation frequency $\Omega_{osci}(x,y) = \sqrt{\Omega_{Rabi}(x,y)^2 + \delta(x,y)^2}$. If the detuning $\delta(x,y)$ is zero (or $\delta(x,y) << \Omega_{Rabi}(x,y)$), the Rabi frequency, i.e., the MW magnetic field, can be extracted by directly fitting the oscillation frequencies. Otherwise, the spatial distribution of the detunings, i.e. the static magnetic field, must be accurately known to derive the Rabi frequency distribution from the oscillation frequencies. So, a prerequisite for using TDRO to get an accurate measurement of the Rabi frequencies is that either the static magnetic field is homogeneous within the imaging region and precisely controlled to let the ground state energy splittings match the input MW frequency, or that the distribution of the static magnetic field is accurately known prior to the TDRO measurements so that it can be used to calibrate the Rabi frequencies. In a low magnetic field case, these prerequisites can be easily achieved by adding compensation coils to maintain a homogeneous magnetic field, and/or by an auxiliary measurement of the static magnetic field [3]. However, in a strong applied magnetic field, as required for imaging at variable frequencies in the tens of GHz range, this is much more challenging to achieve.

2.2 Static magnetic field distribution

In order to image a MW magnetic field of alternative MW frequencies, we need to apply a highly homogeneous and stable static magnetic field to the atoms. In the current setup, we use a pair of permanent magnets to generate the static magnetic field. We recall the schematic of the setup (Fig. 1) and the magnetic field distribution calibration measurement (Fig. 2) from Deliverable 7.2 with a miniaturized cylindrical atomic vapor cell.

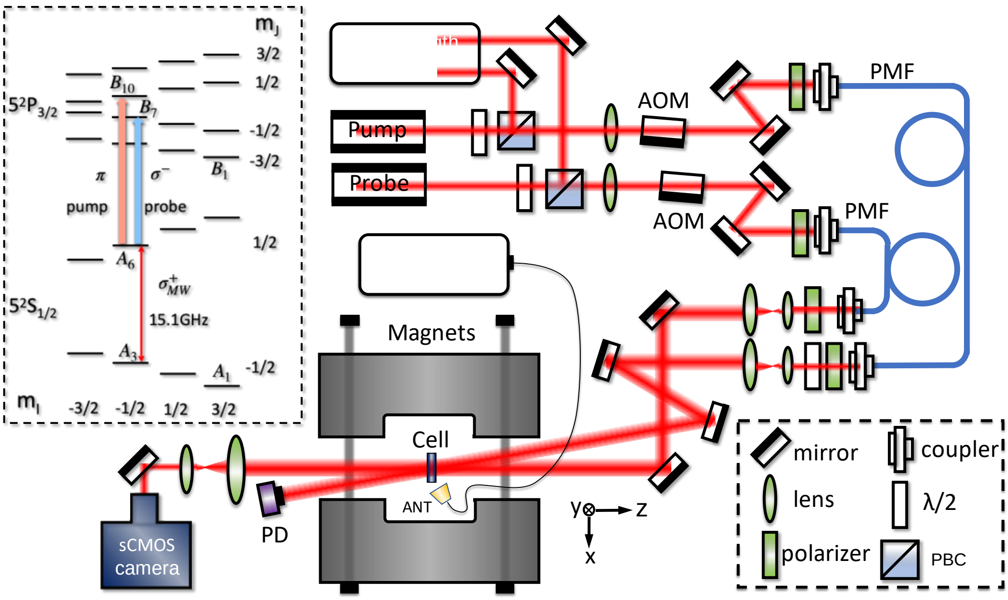

Figure 1: Experimental setup for GHz MW magnetic field imaging

The method we use to image the DC magnetic field distribution is the so-called pulsed double-resonance method [5]. As seen in Fig. 2, in the target MW imaging region (white box), we plotted the pulsed double-resonance measurements of two pixels, showing that the on-resonance MW frequencies are different from the input center MW frequency ($f_{MW}^{center} = 15.1GHz$) by $\delta f_{MW}^{0}(p_1(x,y)) = 5.649(0.020)MHz$ and $\delta f_{MW}^{0}(p_1(x,y)) = 5.608(0.015)MHz$ respectively. Thus the ground state energy splittings between the A_3 and A_6 levels at these two positions are $\omega_0(p_1(x,y)) = 2\pi \cdot \left(f_{MW}^{center} + \delta f_{MW}^{0}(p_1(x,y))\right)$ and $\omega_0(p_2(x,y)) = 2\pi \cdot \left(f_{MW}^{center} + \delta f_{MW}^{0}(p_2(x,y))\right)$ respectively in the current experimental conditions.

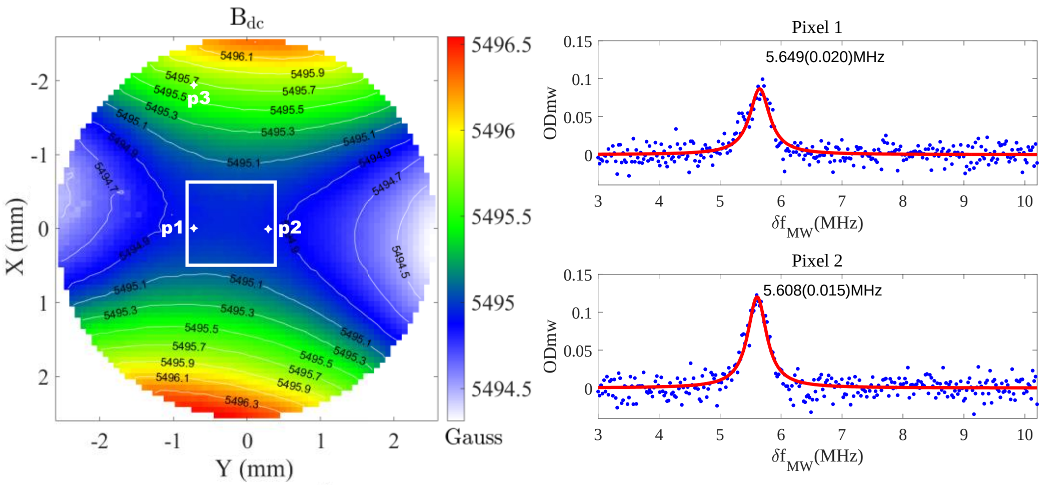

Figure 2: (Left) Static magnetic field distribution of the MW imaging region;

(Right) Pulsed double-resonance measurements to obtain the on-resonance MW frequencies.

We also performed time-domain Rabi oscillation measurements on these two points in a separate measurement, as shown in Fig. 3. The fitted oscillation frequencies from Fig. 3 measurements are $\Omega_{osci}(p_1(x,y)) = 2\pi \cdot 58.7(7)kHz$ and $\Omega_{osci}(p_2(x,y)) = 2\pi \cdot 79.6(4)kHz$, when the input MW frequency is set to be $f_{MW} = 15.1025GHz$.

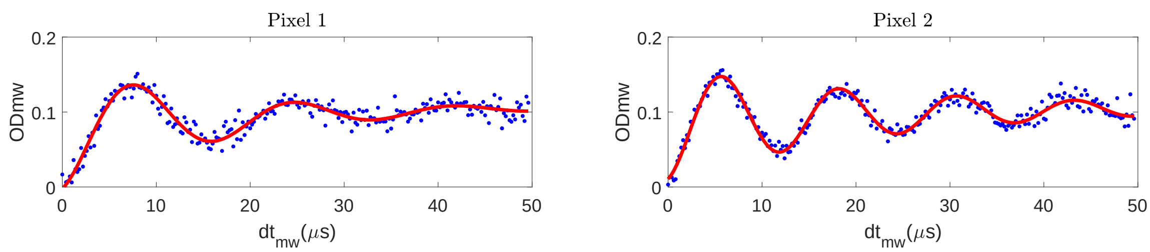

Figure 3: Oscillation frequencies of the two pixels when performing TDRO.

In principle, one can use the detuning values from Fig. 2 to determine the resonant Rabi frequencies with $\Omega_{Rabi}(x,y) = \sqrt{\Omega_{osci}(x,y)^2 - (\omega_0(x,y) - 2\pi \cdot f_{MW})^2}$, if the measurements from Fig.2 represent the detunings for the measurements in Fig. 3. However, since the two measurements are not performed simultaneously and the static magnetic field drifts a bit between the two measurements, extracting the Rabi frequencies from a separate detuning measurement is not practical. Here the DC magnetic field difference between the two measurements is approximately $1Gauss$ and drifting of several Gausses can easily happen within one day. Moreover, we use a 2mm thickness cylindrical cell and the DC field along the laser propagation direction is not homogeneous, as can be seen from the different broadenings of the pulsed double-resonance peaks for these two pixels in Fig. 2, leading to difficulties in finding the accurate detunings of the measurement in Fig. 3.

In summary, the inhomogeneity and instability of the strong DC magnetic field generated by the current setup with permanent magnets are the main limitation and challenges to get an accurate MW field imaging. Alternatively, one should note that a dedicated electromagnet system is commercially available [6], which is able to generate a homogeneous magnetic field in the required MW imaging region size (lateral area: several mm^2), with less than $1ppm$ field drifting in several hours. While still, simultaneous imaging of the Rabi frequencies and detunings is more preferable, which can be achieved by the frequency-domain Rabi spectroscopy method (FDRO) (see Sec. 3).

2.3 MEMS atomic vapor cell

In the macQsimal project, in collaboration with CSEM we designed an ultra-thin MEMS atomic vapor cell (thickness is $200\mu m$) in order to ensure a homogeneous static magnetic field along the laser propagation direction. The MEMS cell is fabricated by CSEM. It has a $15mm \times 30mm$ footprint dimension and is composed of one silicon layer ($200\mu m$ thickness) sandwiched between two glass layers (Fig.4(a,b)). The main working region is a $6mm \times 6mm \times 200\mu m$ measurement cavity, containing pure ^{87}Rb and nitrogen buffer gas. A cylindrical compensation cavity is connected to the measurement cavity via a thin channel. The cell was initially filled with $^{87}RbN_3$ and fabricated by anodic bonding. After shining with UV light, the $^{87}RbN_3$ decomposed into saturated Rb atomic vapor and nitrogen buffer gas. After a careful absorption spectroscopy measurement (Fig.4(c)), the nitrogen buffer gas pressure is found to be $110mbar$ at a temperature of $130°C$, obtained from fitting the buffer gas collisional broadening and shifts of optical transitions of ^{87}Rb based on the Elecsus tool [7].

The MEMS cell also features a $200\mu m$ ultra-thin sidewall, which can be seen in Fig.4(b), enabling a close approach to the MW near field on the MW circuits.

(a) (b) (c)

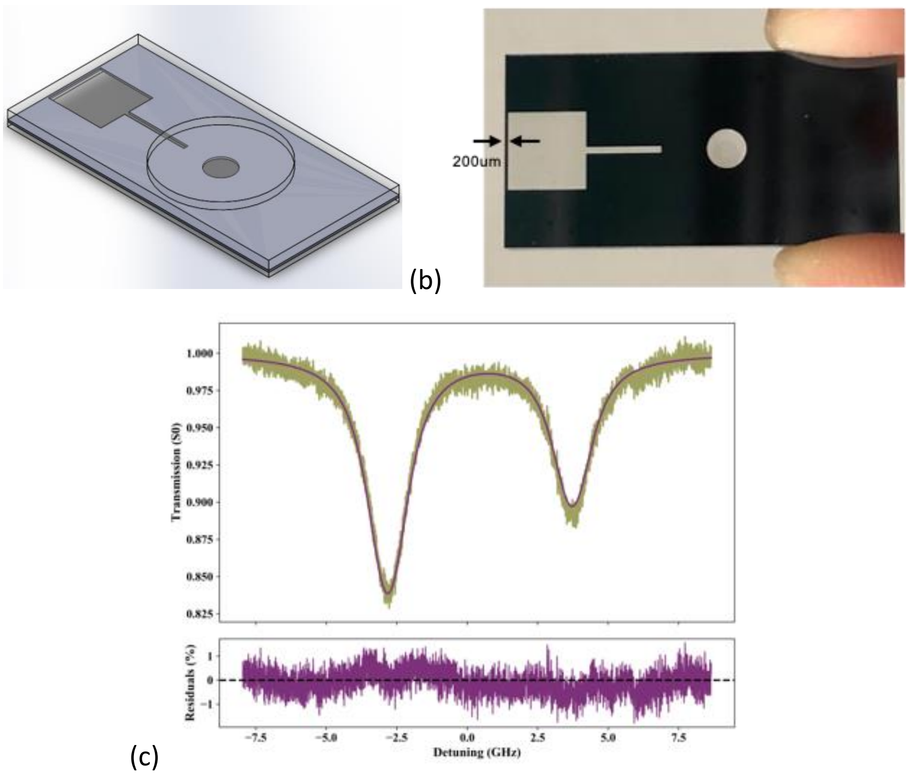

Figure 4: (a) 3D design of the MEMS cell; (b) a close-up of the fabricated MEMS cell; (c) absorption spectroscopy of the MEMS cell to measure the buffer gas pressure (by Elecsus).

3 MW imaging with frequency-domain Rabi spectroscopy

Besides using an ultra-thin MEMS atomic vapor cell, we have developed and implemented an alternative field imaging scheme based on frequency-domain Rabi spectroscopy to measure the Rabi frequencies and detunings simultaneously in a spatially resolved way. Instead of scanning the MW pulse time to extract the time-domain Rabi oscillations, we scan the MW frequency to obtain frequency-domain Rabi fringes on each pixel of the image, from which we can extract the Rabi frequencies and detunings by fitting with a simple model.

As shown in Fig. 5, the pulse sequence of the FDRS experiment is the following: we first optically pump the atoms with a pump pulse, then the MW field is on for a fixed duration t_{MW}, after which a short probe pulse passes through the vapor cell and is captured by the camera to create an actual image; then another pump-probe sequence follows (without the MW) to generate a reference image. By repeating the actual-reference image sequence and comparing the averaged actual image and reference image, we can extract an image of the optical depth change due to the MW (ΔOD_{MW}). By changing the MW frequency for each ΔOD_{MW} image measurement, we can obtain a chain of ΔOD_{MW} images as a function of MW frequencies. Alternatively, we could keep the MW frequency fixed and scan the static magnetic field, which is equivalent as long as the resulting change in detuning is much smaller than the MW frequency. The main difference between the pulsed double-resonance method and the FDRS is the duration of the MW pulse. In pulsed double-resonance method, one usually sets MW pulse time to be much longer than the coherence time such that the population reaches a steady state under MW interaction. While in FDRS, the MW pulse time should be set within the coherence time (typically less than $10\mu s$ for the current vapor cell) to see Rabi dynamics for different MW fields.

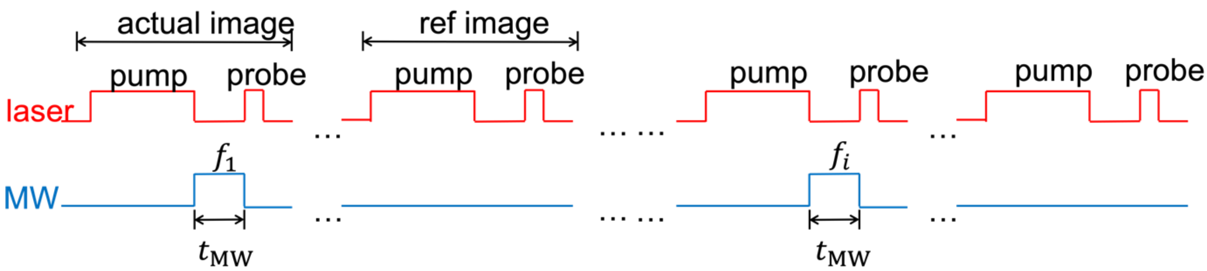

Figure 5: Pulse sequence of the frequency-domain Rabi spectroscopy.

3.1 MW CPW design and fabrication

The Coplanar Waveguide (CPW) is one of the main building blocks of MW circuits, which is mainly used to guide the MW field. It features a homogeneous transmission over a wide MW bandwidth (10s of GHz). Since half of the guiding electromagnetic wave mode is in the air, CPWs are also used to manipulate ultra-cold atoms and to couple MW signals to superconducting qubits. In this work, we design a dedicated CPW structure that fits our field imaging setup and works in high frequency and high temperature (Fig. 6). It is then used as the benchmark circuit to test our FDRS imaging method with ultra-thin MEMS atomic vapor cell. The signal trace width is $694\mu m$ and the gap width (between the signal trace and two ground planes) is $90\mu m$. The bends in the CPW trace are designed to avoid the laser propagation being blocked by the end-launch Sub-Miniature (SMA) connectors.

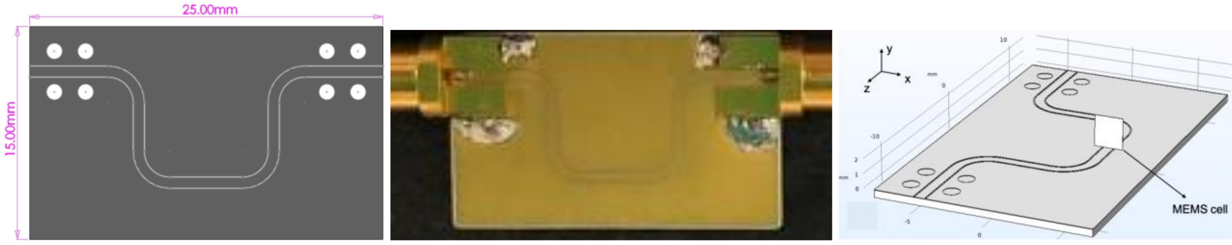

Figure 6: (Left) Top view of the CPW design; (Middle) Top view of the fabricated CPW with End Launch SMA connector; (Right) 3D view of the CPW. The white square is the imaging region of the MEMS cell.

3.2 Imaging results with FDRS

We place the MEMS cell on top of the CPW with the measurement cavity plane orthogonal to the center signal trace of the CPW, as can be seen in the right plot of Fig. 6. The pump and probe laser frequencies are tuned to be on resonance with the corresponding optical transitions shown in Fig. 1. The lasers are guided to propagate along the -z direction. The DC magnetic field is along the x-direction, so the MW magnetic field component that we image is the right-handed circularly polarized component in the yz-plane (the σ_+ MW transition between $A_3 \leftrightarrow A_6$ as shown in Fig. 1).

We design the pulse sequence according to Fig. 5: the pump pulse is $1000\mu s$, the MW pulse is $6\mu s$ and the probe pulse is $1\mu s$. The global exposure time of the camera is $20\mu s$ and set to cover the probe pulse during the whole measurements. After passing through the vapor cell, the pump beam is filtered out to avoid being captured by the camera. The MW frequency array is defined from $15.0522GHz$ to $15.0542GHz$ with a step of $5.013kHz$, so there are in total 400 frequency points (400 measurements). For each measurement, the sequence (in Fig. 5) is repeated 200 times for averaging. The total time for one run of the whole experiment takes around $545s$ (the DC magnetic field fluctuation during this time duration can be ignored).

The measured ΔOD_{MW} images at several example MW frequencies are shown in Fig. 7, representing the local atomic responses (different stages of Rabi oscillations) with the increasing MW frequencies. The evolving "fringe" shape features of the ΔOD_{MW} images can be understood as a consequence of the joint effect from the spatial dependence of the MW magnetic field and the spatial dependence of the DC magnetic field.

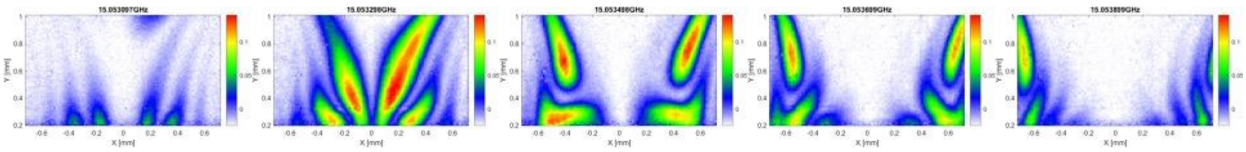

Figure 7: $\Delta \boldsymbol{OD}_{\boldsymbol{MW}}$ image as a function of MW frequencies when performing FDRS.

We then fit the data on each pixel as a function of MW frequency difference δf_{MW} away from the set center frequency $f_{MW}^{center} = 15.0532GHz$, with the following phenomenological model,

$$\Delta OD_{MW}(x,y,\delta f_{MW}) = \boldsymbol{A}(x,y) + \frac{\boldsymbol{\Omega}^2_{\boldsymbol{Rabi}}(x,y)}{\boldsymbol{\Omega}^2_{\boldsymbol{Rabi}}(x,y) + (\boldsymbol{\delta\omega}_0(x,y) - 2\pi\cdot\delta f_{MW})^2} \times \left(\boldsymbol{B}(x,y) + \boldsymbol{C}(x,y)\sin\left(\frac{1}{2}\sqrt{\boldsymbol{\Omega}^2_{\boldsymbol{Rabi}}(x,y) + (\boldsymbol{\delta\omega}_0(x,y) - 2\pi\cdot\delta f_{MW})^2}\cdot t_{MW}\right)^2\right), \qquad (2)$$

where the $\boldsymbol{A}(x,y)$, $\boldsymbol{\Omega_{Rabi}}(x,y)$, $\boldsymbol{\delta\omega}_0(x,y)$, $\boldsymbol{B}(x,y)$, $\boldsymbol{C}(x,y)$ are the fitting parameters, and $t_{MW}=6\mu s$ is the fixed MW pulse duration. The parameter $\boldsymbol{\delta\omega}_0(x,y)=2\pi\cdot\delta f_{MW}^0(x,y)$ is to represent the center frequency of the Rabi resonance. The first term $\boldsymbol{A}(x,y)$ of Eqn. (2) describes an offset of ΔOD_{MW} due to the pumping effect, the $\boldsymbol{B}(x,y)$ in the second term phenomenologically describes a contrast reduction due to the static field inhomogeneity along the laser propagation direction and the remaining part in the second term represents the Rabi dynamics.

Three pixels are selected to show the fitting results (Fig. 8), in which the fit parameters Rabi frequency (Ω_{Rabi}) and detuning ($\delta\omega_0$) are shown, together with the derived MW magnetic field amplitude and the DC magnetic field difference from the value at the center MW frequency ($f_{MW}^{center}=15.0532GHz \leftrightarrow B_{DC}=5474.265Gauss$). From the data one can see that for large MW magnetic field (large Rabi frequency), there are more side peaks in the Rabi fringe, since large Rabi frequency can induce oscillations in large detuned MW frequencies according to $\Omega_{osci}=\sqrt{\Omega_{Rabi}^2+\delta^2}$. Also, the general features of each Rabi spectrum, for example the relative heights between the main peak and all the side peaks, and the splitting of the main peak, are described well by a unique value of the Rabi frequency. Thus, the frequency-domain Rabi spectroscopy can be used to measure the Rabi frequencies accurately.

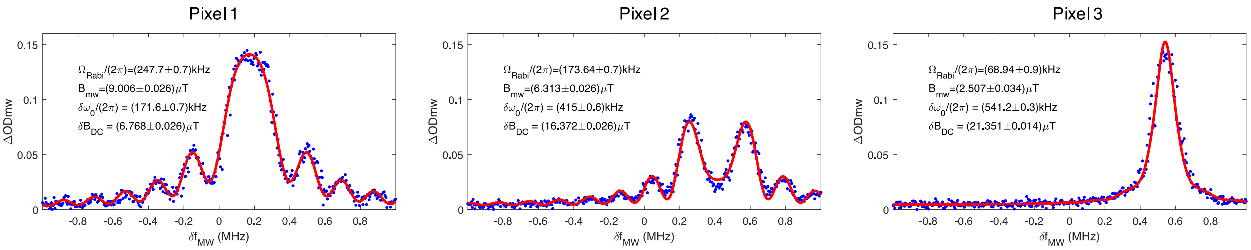

Figure 8: Frequency-domain Rabi spectroscopy measurements and fitting results for three pixels.

Based on the fitting results, we now plot the spatial distribution of the amplitude of the MW magnetic field at around $15.0532GHz$ (Fig. 9). Since the transmission characteristics of the CPW structure don't change within such a narrow frequency band ($2MHz@15.0532GHz$), it is reasonable to assume the MW field distribution doesn't change throughout this bandwidth. The ultra-thin side wall and the CPW (including the signal trace, two ground planes, and a thick substrate) are also illustrated to show the dimension and relative position. From the imaging result, one can see that the near field distribution of σ_+ component of the MW magnetic field (on the yz plane) is a two-lobe shape centered on top of the two gaps of the CPW. Since the z-direction component is rather small, the σ_+ component is similar to the y component, which matches the expected magnetic field line surrounding the signal trace and ground traces.

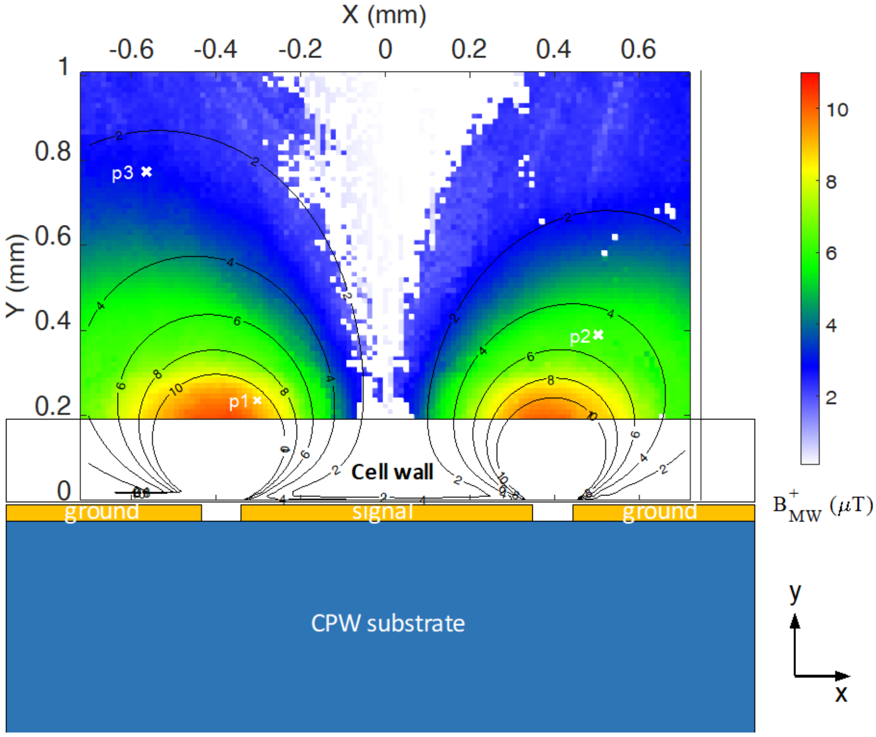

Figure 9: MW ($\sim 15.0532GHz$) imaging results based on FDRS and EM simulation from COMSOL.

To validate our MW imaging results, we performed a full-wave electromagnetic (EM) field simulation with COMSOL software [8]. The result is also presented in Fig. 9 (the solid contour lines and corresponding values). The MW power used in the COMSOL simulation is $0.26W = 24.15dBm$, compatible with the measured MW power coupled into the CPW ($\sim 25dBm$). We can see that the general shape of the measured field distribution matches well with the simulation. The asymmetry of the MW distribution is due to the different area sizes of the two ground planes because of the CPW bends on the board. This asymmetry feature is seen both on the measured and simulated results. The mismatch between the absolute values of measured MW magnetic field amplitudes and the simulated values could arise from fabrication imperfections, from inaccuracies of the simulation (MW power, influence from the surface of the permanent magnet, etc.), or from the static field inhomogeneity along the laser propagation direction. This remains to be investigated in the future.

In addition, we plot the static magnetic field distribution in the same imaging region (Fig. 10), which is calculated from the fitted detunings ($\delta\omega_0$). Note that this DC field distribution is accurately the static magnetic field when Fig. 9 is measured.

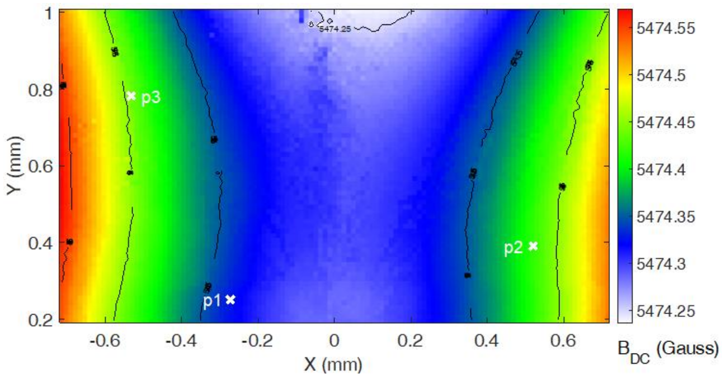

Figure 10: Static magnetic field distribution measured from FDRS.

3.3 Spatial resolution and sensitivity

We now discuss the spatial resolution and MW magnetic field sensitivity of the FDRS method using the MEMS vapor cell in the current experiment. Since the magnetic field is relatively homogeneous within the imaging region (Fig. 10) and our MW pulse time ($6\mu s$) is below the coherence time ($\sim 10\mu s$), coherent features are observed in the measurements. The transverse spatial resolution is then given by the diffusion movement of the Rb atoms in nitrogen buffer gas. At the experimental temperature $T = 141°\text{C}$, the r.m.s. diffusion distance during the MW time can be estimated as $\Delta x = \sqrt{2 \cdot D \cdot t_{MW}} \approx 50\mu m$, where the diffusion coefficient is calculated from $D(Rb\ in\ N_2) = D_0 \frac{P_0}{P_{N_2}} \left(\frac{T}{T_0}\right)^{3/2}$, $P_0 = 1atm$, $P_{N_2} = 110mbar$ is the nitrogen pressure of the MEMS cell, and $D_0 = 0.159cm^2/s$ at reference temperature $T_0 = 60°\text{C}$ [9]. The smallest peak-to-trough feature in one of the ΔOD_{MW} image gives a value of $\sim 80\mu m$ (Fig. 11), which is approaching the r.m.s. diffusion distance. Considering the thickness of the MEMS cell, the spatial resolution of our imaging result is $\sim 80\mu m \times 80\mu m \times 200\mu m$.

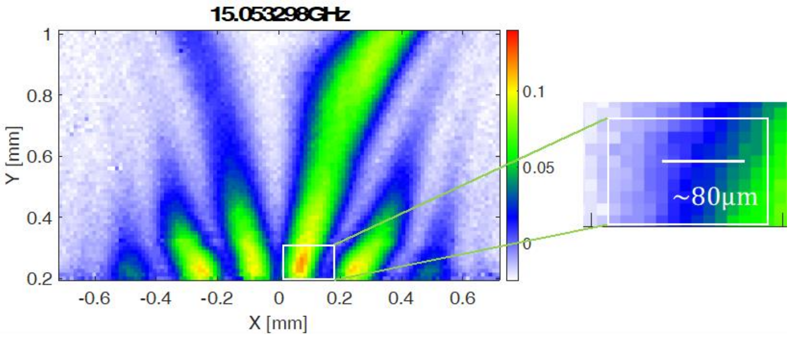

Figure 11: The transverse spatial resolution can be obtained from the smallest peak-to-trough feature in one of the ΔOD_{MW} image ($\sim 80\mu m$).

The MW magnetic field sensitivity can be estimated with fitting errors when performing FDRS. The fitting error is as low as $11.3nT$ for one-pixel block (volume: $12.2\mu m \times 12.2\mu m \times 200\mu m$), considering the total integration time of one measurement ($545s$), the sensitivity is $264nT/\sqrt{Hz}$ at $1Hz$ measurement bandwidth, which is a significant improvement compared with previous measurements [3]. This is even more noteworthy since in the present work, the frequency of the imaged MW field is far away from the ground-state hyperfine splitting of ^{87}Rb, in contrast to [3].

4 Conclusion

In conclusion, we demonstrated a MW magnetic near-field imaging technique based on frequency-domain Rabi spectroscopy, using a compact MEMS atomic vapor cell as an imaging sensor. We validate the technique by imaging the MW near field of a CPW circuit at $f_{MW} = \sim 15.05GHz$. The measured field distribution qualitatively matches with the simulation from a commercial software based on finite-element analysis. The method we use to image the MW field can obtain the static magnetic field simultaneously. The demonstrated spatial resolution is $\sim 80\mu m \times 80\mu m \times 200\mu m$ and sensitivity is $264nT/\sqrt{Hz}$. The method demonstrated here could also be transferred to other MW field imaging systems, for example, using nitrogen-vacancy centers in diamond.

5 References

[1] Böhi, Pascal, and Philipp Treutlein. "Simple microwave field imaging technique using hot atomic vapor cells." Applied Physics Letters 101.18 (2012): 181107.

[2] Böhi, Pascal, et al. "Simple microwave field imaging device." U.S. Patent No. 9,971,000. 15 May 2018.

[3] Horsley, Andrew, Guan-Xiang Du, and Philipp Treutlein. "Widefield microwave imaging in alkali vapor cells with sub-100 µm resolution." New Journal of Physics 17.11 (2015): 112002.

[4] Horsley, Andrew, and Philipp Treutlein. "Frequency-tunable microwave field detection in an atomic vapor cell." Applied Physics Letters 108.21 (2016): 211102.

[5] Horsley, Andrew. "High resolution field imaging with atomic vapor cells". (Doctoral dissertation, University of Basel, Switzerland), 2015.

[6] Private communications with CAYLAR Instrumentation scientifique, (2020). https://www.caylar.net/en/

[7] M. A. Zentile, J. Keaveney, L. Weller, D. J. Whiting, C. S. Adams, and I. G. Hughes, Elecsus: A program to calculate the electric susceptibility of an atomic ensemble, Computer Physics Communications 189, 162 (2015).

[8] https://www.comsol.com

[9] Ishikawa, Kiyoshi, and Tsutomu Yabuzaki. "Diffusion coefficient and sublevel coherence of Rb atoms in N 2 buffer gas." Physical Review A 62.6 (2000): 065401.